# Few-Femtosecond Dynamics of Free-Free Opacity in Optically Heated Metals

A. Niedermayr,[1,*] M. Volkov,[1,2] S. A. Sato,[3,4] N. Hartmann,[1] Z. Schumacher,[1] S. Neb,[1] A. Rubio,[4,5] L. Gallmann,[1] and U. Keller[1]

[1]*Department of Physics, ETH Zurich, 8093 Zurich, Switzerland*
[2]*University of Konstanz, 78457 Konstanz, Germany*
[3]*Center for Computational Sciences, University of Tsukuba, Tsukuba, Ibaraki 305-8577, Japan*
[4]*Max Planck Institute for the Structure and Dynamics of Matter, Luruper Chaussee 149, 22761 Hamburg, Germany*
[5]*Center for Computational Quantum Physics (CCQ), Flatiron Institute, New York 10010, New York, USA*

(Received 1 June 2021; accepted 15 March 2022; published 25 May 2022)

Interaction of light with an excited free-electron gas is a fundamental process spanning a large variety of fields in physics. The advent of femtosecond laser pulses and extreme-ultraviolet sources allowed one to put theoretical models to the test. Recent experimental and theoretical investigations of nonequilibrium aluminum, which is considered to be a good real-world representation of an ideal free-electron metal, showed that, despite significant progress, the transient hot-electron/cold-ion state is not well understood. In particular, the role of plasmon broadening, screening, and electron degeneracy remains unclear. Here, we experimentally investigate the free-free opacity in aluminum on the few-femtosecond timescale at laser intensities close to the damage threshold. Few-femtosecond time resolution allows us to track the purely electronic contribution to nonequilibrium absorption and unambiguously separate it from the slower lattice contribution. We support the experiments with *ab initio* calculations and a nearly free electron model in the Sommerfeld expansion. We find that the simplest independent-particle model with a fixed band structure is sufficient to explain the experimental findings without the need to include changes in screening or electron scattering, contrasting previous observations in 3*d* transition metals. We further find that electronic heating of a free-electron gas shifts the spectral weight of the absorption to higher photon energies, and we are able to distinguish the influence of the population change and the chemical potential shift based on the comparison of *ab initio* calculations to a simplified free-electron model. Our findings provide a benchmark for further investigations and modeling of dense nonequilibrium plasma under even more extreme conditions.

DOI: 10.1103/PhysRevX.12.021045 Subject Areas: Condensed Matter Physics, Optics

## I. INTRODUCTION

Photon absorption by free electrons in metals, warm dense matter, and plasmas is a longstanding fundamental problem that plays an essential role in laser-matter interactions [1,2]. Despite our excellent understanding of photoabsorption mechanisms on the attosecond timescale by bound electrons in dielectrics [3,4], semiconductors [5], and metals [6], the role of free electrons is still actively debated [7–9]. Both theoretical and experimental challenges contribute to this problem. Absorption by bound, localized electrons from specific atomic shells is successfully described, in most cases, by an electron-hole pair in the mean field of other nonparticipant charges. In contrast, absorption by delocalized and degenerate electrons is inherently a many-body problem, where the effects of dynamical screening and electron correlation generally need to be considered [10].

Experimental evidence that could unambiguously test the various theoretical approximations to the many-body problem is difficult to obtain because the majority of experimentally accessible physical systems are either bound-electron or nondegenerate systems. Under laboratory conditions, intense laser pulses can transiently create a phase transition from a solid state to a nonequilibrium plasma [11]. However, it is hydrodynamically unstable and notoriously difficult to characterize [11]. As an alternative, metallic aluminum has been used as a more convenient test system [9,12–15]. It approximates the behavior of an ideal free-electron gas very well [10] in the extreme-ultraviolet (XUV) transparency window between its plasma frequency (15 eV) and the $L_{2,3}$ absorption edge (72–74 eV). In this

*To whom correspondence should be addressed: niedermayr@phys.ethz.ch

sense, aluminum serves as a testbed for fundamental light-matter interactions in such materials, in particular, for free-free absorption. Furthermore, aluminum is widely used as a near-infrared (NIR) blocking filter in tabletop high harmonic generation (HHG) sources for the generation of XUV light and, thus, of general interest for the community.

Measurements of equilibrium absorption provide crucial, but limited insight because of electron-lattice coupling, whereas time-resolved investigations of free-free absorption in nonequilibrium aluminum are scarce. Two recent studies [7,16] of nonequilibrium, hot-lattice aluminum utilizing free-electron laser and high-harmonic sources have resolved some of the discrepancies between experiment and theory, which in these cases, were based on time-dependent density functional theory (TDDFT) and a model based on the random phase approximation (RPA) framework. Specifically, the former study used an *ad hoc* screening potential to explain the absence of change in XUV absorption in the hot-electron state. In addition to screening, the latter study discussed the possibility of plasmon broadening and electron degeneracy affecting XUV absorption on the femtosecond timescale [16]. However, the results reported so far on the hot-electron/cold-lattice state were inconclusive because of the lack of temporal resolution and sensitivity.

Here, we use attosecond transient absorption spectroscopy supported by *ab initio* calculations to address the coupling of XUV light to the free electrons in the transition regime from the cold-lattice to the hot-lattice state. Unambiguous separation of electronic and lattice contributions in the experimental data allows us to gauge the physical mechanisms that can be further explained by a simplified theoretical model.

## II. RESULTS AND DISCUSSION

### A. Equilibrium absorption

Our experimental approach draws on our recent investigation of laser-excited titanium on the attosecond timescale [6], where strong bound-electron effects dominate. Aluminum, in contrast, exhibits the opposite, free-electron character in the same photon energy range. The experimental apparatus is described in detail in the Appendix A and in previous work [17]. Figure 1(a) (blue line) shows the equilibrium absorption coefficient of a 200-nm free-standing polycrystalline aluminum foil (Lebow Co.) measured with attosecond pulse trains (APTs) in the range from 25 eV to 77 eV (see Appendix C for details). Our data are in good agreement with the reported values for thin aluminum foils with a few-nm oxide layer (black points in Fig. 6 from Ref. [13]).

We compare the experimental data with *ab initio* calculations of the aluminum absorption obtained with TDDFT in the local density approximation. Because we freeze ions in the TDDFT calculations at their equilibrium positions and ignore electron-electron scattering in the mean-field approximation, they exhibit more structure than the experimental data. To efficiently account for the electron-phonon and electron-electron scattering that

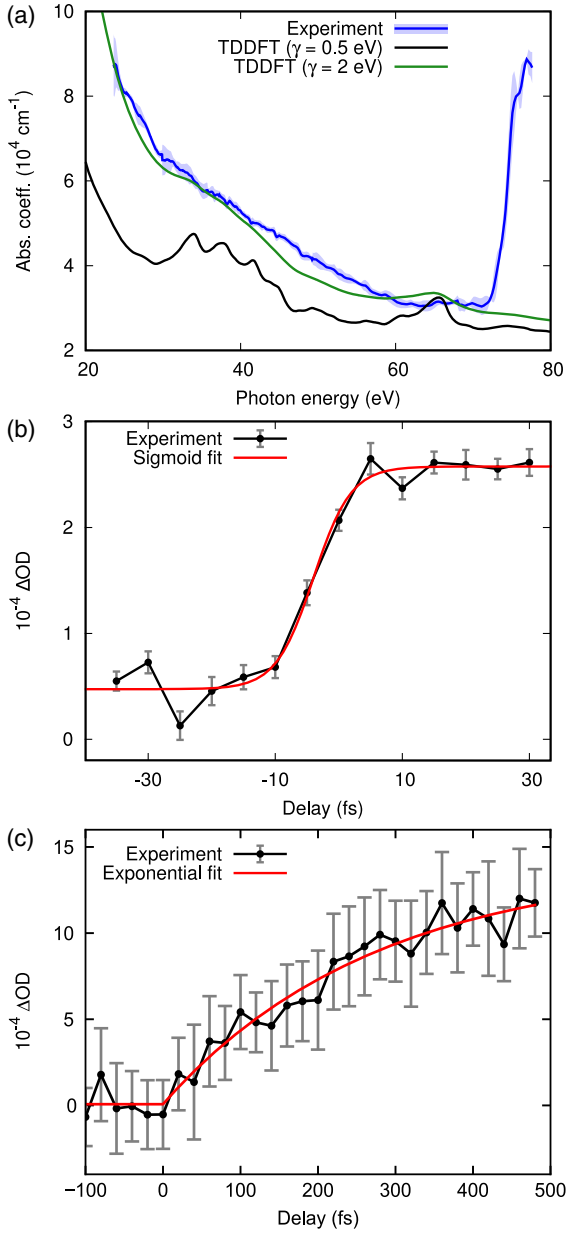


FIG. 1. (a) Measured absorption coefficient of aluminum (blue line; the standard error is shaded) compared to TDDFT calculations with different line-broadening parameters (green line = 2 eV, black line = 0.5 eV). No core-level absorption was taken into account for TDDFT at 73 eV. (b,c) Optical density change ΔOD between 42 eV and 44 eV after NIR excitation (black line; gray bars show standard error). (b) Few-femtosecond dynamics, reflecting the electronic heating. The absorbed laser fluence is fitted with a sigmoid function to the optical density change (red line) with a rise time of 13.0 ± 3.2 fs. (c) Subpicosecond lattice response (black line) and an exponential fit (red line) with a response time of 274 ± 62 fs.

occurs, we increase the linewidth broadening from 0.5 eV to 2 eV [Fig. 1(a), black line to green line]. This provides the best fit to the experimental data. The physical meaning of the linewidth broadening parameter is the inverse lifetime of the electronic states or their generalized collision frequency. Both the electron-phonon and electron-electron scattering rates are expected to be unaffected by the pump excitation because for the former effect the lattice system is not heated yet and for the latter effect the population change around the Fermi level has little influence on the lifetime of high-energy electron-hole pairs. The required broadening is higher than typically used, e.g., in the Drude model [18] because the electrons are excited to very high-lying states that exhibit strong scattering and thus are prone to a fast decay. Note also that the present calculation does not capture the $L_{2,3}$ absorption edge at 73 eV since the core levels are frozen with the pseudopotential approximation.

### B. Nonequilibrium absorption

#### 1. Experimental results

We use a pump-probe setup [17] to investigate transient changes in the XUV absorption of our aluminum samples after excitation with a 13 fs NIR pulse with a center photon energy of 1.59 eV, a peak intensity of $3.8 \times 10^{11}$ W/cm$^2$, and a pulse energy of 1.1 $\mu$J. By keeping the pump intensity below $5.5 \times 10^{11}$ W/cm$^2$, we avoid irreversible changes to the material and thus perform multishot experiments in a well-characterized sample. The change in absorption is probed with XUV pulse trains in the range from 30 eV to 50 eV. The pulse trains are produced by high-harmonic generation in argon and have an average pulse duration of 270 as, while the sample response in this particular study is limited by the 13 fs pump pulse (see Appendix C for details). The zero delay and cross-correlation between the NIR and XUV pulses are obtained from a two-photon, two-color photoemission experiment in neon [19,20]. The XUV probe spectrum is shown in Fig. 2(a). The 2-eV broad integration window roughly corresponds to the spectral coverage of an individual harmonic.

The transient modification of the optical density due to NIR excitation is displayed in Figs. 1(b) and 1(c) on two different timescales: on a few-fs timescale, corresponding to characteristic electronic heating times; and on a subpicosecond timescale, corresponding to characteristic lattice heating times. Positive delays mean that the pump laser precedes the probe beam. On both timescales, we observe an increase in absorption and a very similar qualitative response across the studied 30 eV to 50 eV photon energy interval (see Figs. 9 and 10 in Appendix E). Thus, we average the XUV signal between 42 eV and 44 eV over an individual harmonic with a width of about 2 eV (see Appendix B). We note that for the separation of the electronic and lattice response, prior knowledge of a substantial difference in their characteristic timescales is necessary. Such knowledge can, for example, be obtained via direct measurements such as ultrafast electron diffraction [21].

On the few-femtosecond timescale, the increase in optical density instantaneously follows the laser fluence within the resolution of our experiment, exhibiting a pronounced step-function shape with a rise time of $13.0 \pm 3.2$ fs from 10% to 90% of the amplitude of the fitted curve (see Appendix E). This rise time is in good agreement with the NIR-XUV cross-correlation width (see Appendix C). The few-femtosecond reaction is followed by a slower and stronger response [see Fig. 1(c)], with a characteristic timescale of $274 \pm 62$ fs. The behavior on this timescale is attributed to the aluminum lattice response that shows a comparable 350 fs response time in femtosecond electron diffraction experiments under similar excitation conditions [21]. Such a distinct separation of the electronic and the lattice response has not been shown previously in the free-free absorption range of aluminum.

Although our attosecond transient absorption technique allows us to resolve field-driven subcycle oscillations of the optical density in dielectrics [4] and semiconductors [5] at similar pump intensity with attosecond pulse trains, no oscillations are observed in aluminum with a sensitivity of about $4 \times 10^{-3}$ OD, which is, however, about 2 orders of magnitude worse than the sensitivity of our coarse scans presented in Fig. 1(b) (see Appendix D). This is expected because of the short lifetime of the XUV-excited electrons, corresponding to the estimate of 2 eV for spectral broadening as derived from our equilibrium absorption measurements.

#### 2. Ab initio calculations

The clear separation between electronic and lattice responses allows us to compare the data with frozen-lattice TDDFT calculations that exclusively model the electronic response. The electron-electron thermalization time at similar optical excitation is less than 11 fs [22], and aluminum has no $d$-orbitals around the Fermi level. Therefore, to model the hot-electron state, we assume a Fermi-Dirac distribution. In order to mimic the 16-nm absorption depth of the NIR laser in a 200-nm aluminum foil, we employ a spatially dependent temperature profile with a peak electron temperature of 7000 K at the sample surface (see Appendix G).

Figure 2 compares the calculated (blue line) and measured (gray dots and green markers) spectral profiles of the optical density change $\Delta$OD in the hot-electron/cold-lattice state. The measurement is taken at a delay of +20 fs after the NIR pulse is absorbed but before any signs of lattice thermalization appear. We note that, in this study, we do not analyze the region of temporal pump-probe overlap in detail. The experimental data are a weighted average over 45 measurements, with the details on the averaging procedure described in Appendix B. In Fig. 2(a), we subtract the energy-dependent background at negative delays before the pump-probe overlap in order not to

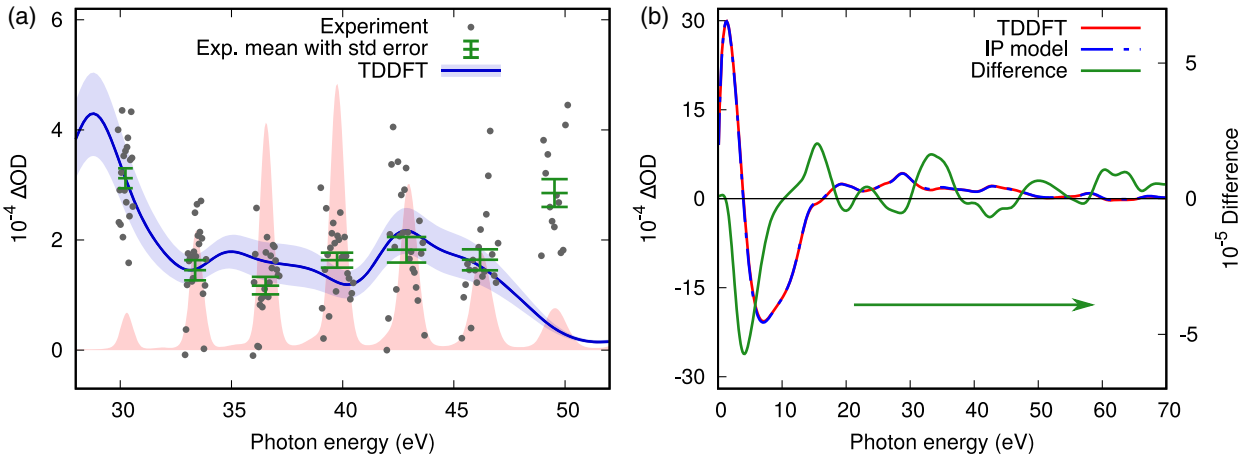


FIG. 2. Spectrally resolved change in optical density of aluminum, recorded at a delay of 20 fs, corresponding to a hot-electron/cold-lattice state. (a) Individual measurements (gray dots) and their spectral average, with the standard error over individual harmonics (green markers), shown at a fixed pump-probe delay of 20 fs and exhibiting an increase in optical density ΔOD towards lower photon energies. The red-shaded area in the background corresponds to the XUV probe spectrum. The TDDFT calculations (blue line) were computed by increasing the electron temperature to 7000 K and taking the difference of the absorption coefficient between the hot- and cold-electron states. (b) Full TDDFT (red line) and IP calculation (dashed blue line).

account for the signal from previous pulses. The TDDFT calculations agree well with the measurements in the probed energy range from 30 eV to 45 eV. To account for pulse energy fluctuations and beam drifts during the measurements, we vary the electronic temperature by ±20% of the excess energy of aluminum in the TDDFT calculations. At 49 eV, the calculations underestimate the measured absorption change by a factor of 3 [see Fig. 2(a)]. The origin of the discrepancy between experiment and theory at 49 eV is not easy to identify. A potential reason for the discrepancy may be the surface oxidization of the sample. In the theoretical calculations, we consider a perfect aluminum thin film, but the sample has an oxidized surface. The surface layers may have a larger contribution to the transient absorption than layers further away from the surface because the highest amount of energy is deposited at the surface.

## C. Discussion

### *1. Comparison with previous XUV transient absorption studies*

In the following, we briefly summarize our main observations and compare them with our previous findings on few-femtosecond absorption dynamics in titanium [6]. In aluminum, we observe a relatively weak ($\Delta OD \sim 2 \times 10^{-4}$) and spectrally homogeneous (over multiple 10 eV) stepwise increase in absorption within the error bars on the few-femtosecond timescale. While we have observed a similar few-femtosecond stepwise increase in XUV absorption in titanium, its spectral response is highly inhomogeneous and has a fundamentally different nature. The induced absorption change is about 2 orders of magnitude larger in titanium and shows a pronounced resonance profile in its spectral response. In contrast to aluminum, titanium exhibits localized $3d$ states at the Fermi level and thus strongly deviates from the free-electron model.

In titanium, the XUV photoabsorption is shaped by three different effects, namely, Pauli blocking, screening, and broadening [6]. The latter two effects change the photoabsorption line shape around the titanium giant resonance, masking the effect of Pauli blocking. For aluminum, in the same XUV photon energy range, screening and broadening contributions are weak because of the low density of states (DOS) of bound $d$- and $f$-electrons, allowing Pauli blocking to manifest distinctly during electronic heating.

This different behavior in aluminum can be attributed to its "ideal" metal nature, with its valence electrons moving freely and its ionic potential completely screened. This nature is confirmed in quantitative convergent-beam electron diffraction experiments that show a highly homogeneous electron density and tetrahedrally centered bonding [23]. Angle-resolved photoemission experiments also show a free-electron dispersion of the valence band [24]. The most significant deviations from a free-electron structure arise at 1.5 eV due to parallel-band resonance [25] and at 28 eV due to a pseudogap between resonant states exhibiting localized $d$- and $f$-states in the partial-wave components of the density of states [26]. However, our XUV probe pulses do not overlap with the parallel-band resonance, and the NIR excitation cannot populate the localized pseudogap states. Figure 3(c) shows the band structure of aluminum along the symmetry directions [27].

Furthermore, it is worth noting that in aluminum and with our experimental parameters, the NIR excitation does not overlap with the final states of the XUV excitation. This is due

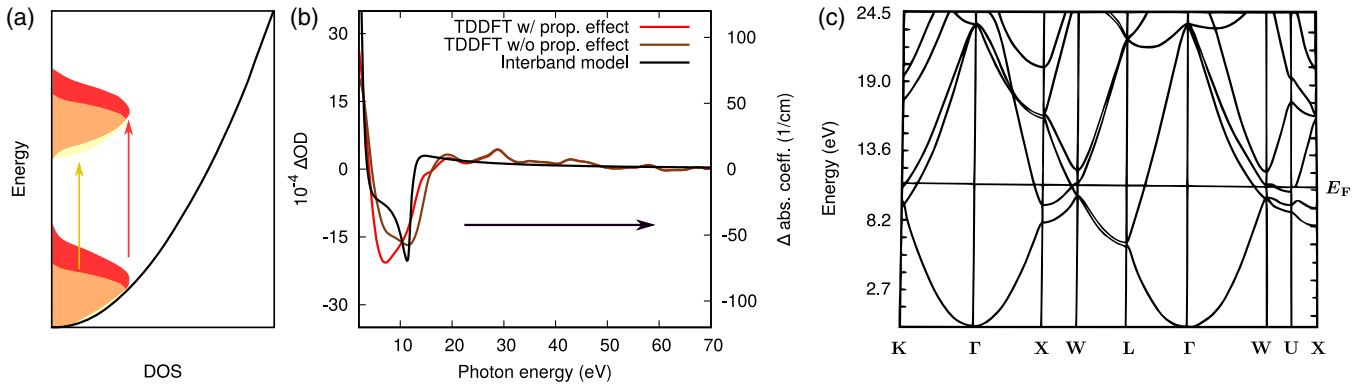


FIG. 3. (a) Schematic representation of the global increase in free-free absorption. Yellow stands for the nonexcited quasifree electron gas, and red for the excited electron gas. The vertical arrows correspond to the probe transition of the nonexcited or excited electron gas, while the pump is responsible for the broadening or heating of the electron distribution. Excitation by the NIR pump shifts the initial XUV states to higher energies. Thus, via the XUV probe transitions, final states will also be occupied at higher energies by pump-excited electrons compared to nonexcited electrons. Since the transition probability is given by the product of filled initial and empty XUV final states (Appendix L), there is a net increase in absorption for high photon energies because the DOS of a free-electron gas scales as the square root with energy. In panel (b), the brown (red) line shows the change in optical density predicted by the TDDFT calculations without (with) the propagation effect and surface reflection of the electromagnetic field included. The black line corresponds to a simple interband model, which includes the chemical potential shift. It leads to a decrease of absorption around the Fermi level and is in good qualitative agreement with the TDDFT calculations without propagation effects included. The chemical potential change (−26 meV) was calculated for an initial temperature of 300 K and a final temperature of 7000 K. The interband model is described in more detail in Appendix L. Panel (c) shows the band structure of aluminum along the symmetry directions.

to the fact that the valence band of aluminum is 11 eV wide [26], and the lowest transition energy covered by the XUV in our experiment is around 30 eV.

### 2. Independent-particle model and the Sommerfeld expansion

To exclude dynamical many-body effects as the origin of the electronic response, we compare the full TDDFT calculations with the independent particle (IP) model, where electrons are treated independently and collective effects like electron interactions or screening are excluded. Thus, the IP absorption model includes only the change of the state occupation, while the band structure is kept fixed under excitation. Figure 2(b) compares the full TDDFT calculation with the IP calculation, yielding excellent agreement. The difference between the two curves is shown by the green line and amounts to only a few percent of the observed absorbance change. Since the full TDDFT calculation and the independent particle model show an excellent agreement, we conclude that the change in optical density stems from the occupation change alone.

To further analyze our results, we revisit the nearly free electron model in the Sommerfeld approximation. In particular, we include the perturbation of the periodic lattice to the Hamilton operator of a free-electron gas as an external potential. We then calculate the temperature dependence of the real part of the optical conductivity, which is directly proportional to the absorbance. Taking the difference of the optical conductivity of the hot- and the cold-electron gas is thus directly linked to the time-dependent absorption. The details of the calculations are given in Appendix J. We obtain that, for electronic wave vectors $|\mathbf{G}| > 2\ \mathrm{k}_F$ ($\mathrm{k}_F$ corresponds to the radius of the Fermi sphere of the free-electron gas), the probe transition from the initial state $|\boldsymbol{k}\rangle$ to the final state $|\boldsymbol{k}+\boldsymbol{G}\rangle$ has a positive contribution to the change of optical absorption with increasing temperature; for $|\mathbf{G}| < 2\ \mathrm{k}_F$, the contribution is negative. Larger values of $|\mathbf{G}|$ correspond to the absorption of higher-energy XUV photons.

We can attribute the change in photoabsorption to two effects: The increase in electron temperature smears out the Fermi-Dirac distribution, which causes a global increase of absorption at all photon energies between the plasma frequency and the L-edges. This can be explained by the general equation of the XUV transition probability, which is proportional to the product of initial density of states and initial electron distribution [Fig. 3(a), Appendix L]. The NIR excitation shifts the electron population to higher energies, and since the density of states scales as the square root with energy for a free-electron gas, the transition probability is increased for photon energies above the Fermi level at 11.7 eV. Such a global enhancement of absorption over multiple tens of eV is uncommon in rare-earth and transition metals because of the non-negligible presence of localized $d$- or $f$-electrons and the resulting, considerably more structured, density of states.

The second effect is governed by the change of the chemical potential due to the change of the temperature of

the electron gas. An increase in electron temperature leads to a reduction of the chemical potential. This, in turn, leads to a reduction of the number of electrons below the Fermi level that take part in the light-matter interaction, and thus, the optical conductivity is reduced. This effect is most pronounced for particle energies close to the Fermi level. If we take into account the plasmon resonance for the macroscopic optical response of the metal film and, more specifically, its change due to the NIR laser-induced electron-gas heating, we find that, in aluminum, the minimum of the negative response is shifted by about 5 eV to lower energies because of the positive contribution from the plasmonic response. However, the net negative transient absorption change sets in at the same upper photon energy of about 15 eV.

We would like to point out that the inclusion of electron-electron and electron-phonon scattering is important to describe the ground-state absorption at room temperature. However, our main observable is the change in the optical density that happens at a constant lattice temperature; thus, electron-phonon scattering does not contribute to the change in the investigated timescale. It is, in principle, possible that the generalized collision frequency increases as more scattering channels become available after partial removal of the degeneracy due to the heating of the electron gas. However, that would be a second-order effect on top of the basic population change. Since we find that the population change alone is sufficient to explain the experiment, this indirectly proves that the other effects must be small in comparison.

To summarize, the photoabsorption decreases for low and increases for high probe photon energy with possible modification due to the plasmonic response. The response found at high photon energies is confirmed by our experimental findings and the overall behavior by the TDDFT calculations. Note that the photon energy range where theory predicts a decrease in absorption is not accessible in our experiments. In previous semiconductor studies electron heating or electron population mapping was observed through spectral shifts of the absorption edges [28,29]. Our findings reveal a basic but novel aspect of metallic electronic systems.

## III. CONCLUSION AND OUTLOOK

Few-femtosecond time resolution enabled the measurement of free-free absorption of aluminum in a cold-lattice state, thereby allowing a direct comparison with TDDFT and IP calculations. We have found that electron heating in a degenerate electron gas leads to two competing mechanisms: the electron distribution smearing and the chemical potential shift. The first effect leads to a global enhancement of absorption at all photon energies in the free-free absorption range. In contrast, the chemical potential shift leads to a decrease in absorption, which is most pronounced close to the Fermi level. This global and universal intrinsic response is superimposed by the material-specific plasmon resonance in the macroscopic signal.

In previous studies [7,9,12], it was shown that theoretical models—including inverse bremsstrahlung, RPA, and DFT—were not able to consistently describe the cold- and hot-electron states of aluminum. Additionally, an experimental study [15] stated that little or no change in absorption is observed upon electron heating by 1 eV. They proposed that different mechanisms—like plasmon broadening, plasma screening, and electron degeneracy—were responsible for deviations between the experimental and theoretical results. Although we excited the sample at much lower peak intensities of $3.8 \times 10^{11}$ W/cm$^2$, we could quantitatively characterize the nonequilibrium free-free absorption in a cold-lattice state. We were able to explain our experimental findings by separation of the chemical potential shift, the fixation of the band structure, and the exclusion of degeneracy effects.

The observed effects are universal in the sense that they are present in all materials with a finite number of free carriers like metals. However, in materials with a more complex electronic structure, they may be masked by other, stronger contributions. With this study, we further complete the picture of NIR absorption in metals. Because of the similarities of free-electron-like metals with dense plasmas, this work may also provide a missing benchmark for improving our understanding of dense nonequilibrium plasma with higher electron temperature and for calibration of corresponding models.

## ACKNOWLEDGMENTS

This research was supported by the NCCR MUST, funded by the Swiss National Science Foundation (SNSF) and by SNSF Project No. 200020_172644. Z. S. gratefully acknowledges support from the ETH Zurich Postdoctoral Fellowship Program. This project has received funding from European Union's Horizon 2020 under MSCA Grant No. 801459, FP-RESOMUS. This work was supported by JSPS KAKENHI Grant No. JP20K14382, the European Research Council (ERC-2015-AdG694097), the Cluster of Excellence "CUI: Advanced Imaging of Matter" of the Deutsche Forschungsgemeinschaft (DFG)—EXC 2056—Project ID No. 390715994, Grupos Consolidados UPV/EHU (IT1249- 19), partially by the Federal Ministry of Education and Research Grant No. RouTe-13N14839, and the SFB925 "Light induced dynamics and control of correlated quantum systems." The Flatiron Institute is a division of the Simons Foundation.

## APPENDIX A: EXPERIMENTAL METHODS

Figure 4 shows the attosecond transient absorption spectroscopy (ATAS) setup that is extensively described in Ref. [17]. A commercial Ti:sapphire laser system provides about 25-fs laser pulses with a repetition rate

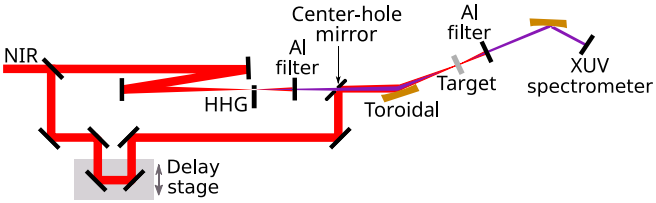


FIG. 4. Sketch of the attosecond transient absorption spectroscopy (ATAS) setup. The pump (NIR) and probe (XUV) beams are recombined with a center-hole mirror and focused on the target by a toroidal mirror. The transmitted XUV spectra are recorded with an XUV spectrometer. Both aluminum filters have a thickness of 100 nm.

of 1 kHz. The pulses are further shortened to 13 fs with an argon-filled two-stage filament compressor. The employed pulse duration yields an optimum balance between spectral width and stability of the generated XUV spectrum. The compressed pulses have a center wavelength of 780 nm and a pulse energy of 300 $\mu$J. The laser beam is divided into a pump and probe arm by an 80:20 beam splitter. The more energetic pulse produces XUV (probe) pulses by HHG in argon. After HHG, the residual fundamental beam is blocked with a 100-nm-thick aluminum foil. The weaker pulse is used as the pump in our experiment. The pump path contains a delay stage and a mechanical shutter. The pump and probe beams are recombined by a center-hole mirror and focused on the target sample with a toroidal mirror. A copropagating continuous-wave laser beam at 473 nm is used to actively stabilize the pump-probe delay. Polycrystalline aluminum foils (Lebow Co.) mounted on copper TEM grids with 7 windows, with a diameter of 500 $\mu$m each, are used as the sample in this study. The pump and probe beams are focused by a toroidal mirror (Carl Zeiss Laser Optics GmbH) on the freestanding window with $1/e^2$ focal diameters of approximately 230 $\mu$m and 50 $\mu$m, respectively. As a result, the pump illumination can be considered transversely homogeneous across the probe focal spot.

The XUV spectra transmitted through the sample are recorded by an XUV grating spectrometer (McPherson Model 251). The spectrally dispersed XUV beam is detected with a CCD camera (PIXIS-XO, 400B, Princeton Instruments). The shutter in the pump arm is used for fast data acquisition of subsequent spectra without and with a pump beam on the sample for each pump-probe delay step. This fast-referencing approach increases the signal-to-noise ratio (SNR) and allows us to detect transient absorption changes well below 1%. Before and after transient absorption scans, the static absorption of the sample is measured to ensure that the samples are not irreversibly modified by the laser. To increase the SNR of the static absorption scans, the aluminum sample was moved in (signal) and out (reference) of the XUV beam multiple times during a single measurement. Additionally, transient absorption measurements were carried out on different days and on different positions on the sample to ensure reproducibility.

## APPENDIX B: OPTICAL DENSITY CALCULATION

The pump-induced change in optical density $\Delta\mathrm{OD}(E,t)$ is defined as

$$\Delta\mathrm{OD}(E,t) = \ln\frac{I_{\mathrm{XUV\,only}}}{I_{\mathrm{XUV+IR}}(t)}, \tag{B1}$$

where $I_{\mathrm{XUV\,only}}$ and $I_{\mathrm{XUV+IR}}$ represent the transmitted probe spectral intensities without and with pump excitation, respectively. Here, $t$ is the pump-probe delay with the convention that positive delays correspond to the probe pulse arriving after the pump pulse, and $E$ represents the probe photon energy.

The measured transient optical density $\Delta$OD data shown in the main manuscript are calculated as a weighted average over multiple measurements with a similar procedure to the one described in Ref. [6]. Each measurement $i$ consists of multiple pairs $j$ of spectra with (signal) and without a pump (reference) recorded at each delay step $k$. The weighted optical density at each delay step $k$ reads as

$$\Delta\mathrm{OD}_k = \frac{\sum_i w_{i,k}\Delta\mathrm{OD}_{i,k}}{\frac{n-1}{n}\sum_i w_{i,k}}, \qquad w_{i,k} = \frac{1}{\sigma_{i,k}^2}, \tag{B2}$$

where $w_{i,k}$ stands for the weighting coefficients within a measurement $i$ for each delay step $k$, given as the inverse squared of the standard deviation. The standard deviation squared $\sigma_{i,k}^2$ for each individual measurement $i$ and each delay step $k$ is given by

$$\sigma_{i,k}^2 = \frac{\sum_i (\Delta\mathrm{OD}_{j,i,k} - \langle\Delta\mathrm{OD}\rangle_{i,k})^2}{N-1}, \tag{B3}$$

where $j$ is the index for each signal-reference pair and $\langle\Delta\mathrm{OD}\rangle_{i,k}$ corresponds to the mean value of $\Delta\mathrm{OD}_i$ within one delay step $k$ for a single measurement $i$.

The uncertainty of the change in optical density is given by

$$\sigma_{\Delta\mathrm{OD}_k}^2 = \frac{\sum_i (\Delta\mathrm{OD}_{i,k} - \Delta\mathrm{OD}_k)^2}{\frac{n-1}{n}\sum_i w_{i,k}}. \tag{B4}$$

Finally, the total change in optical density is averaged over finite energy slices of approximately 2 eV in width (which corresponds to the width of individual harmonics) weighted with the inverse square of the standard deviation of the individual energy slices $l$. The total change in optical density reads as

$$\Delta\mathrm{OD}_{\mathrm{tot},k} = \frac{\sum_l w_{l,k}\Delta\mathrm{OD}_{l,k}}{\frac{n-1}{n}\sum_l w_{l,k}}, \qquad w_{l,k} = \frac{1}{\sigma^2_{\Delta\mathrm{OD}_{l,k}}}, \tag{B5}$$

where $l$ corresponds to a discrete energy value of the change in optical density $\Delta\mathrm{OD}_k$.

## APPENDIX C: PULSE CHARACTERIZATION AND RECONSTRUCTION

The attosecond pulse trains used in the experiments cover the photon energy range between 25 eV and 55 eV [Fig. 5(a)]. We characterize both the XUV and the infrared pulses using the reconstruction of attosecond beating by interference of two-photon transitions (RABBITT) technique in neon gas [19,20]. Four oscillating sidebands are visible in the photoelectron spectrum, showing a small attochirp [black line in Fig. 5(b)]. We extract the phase difference of the individual sidebands and interpolate them linearly; thus, the femtochirp [30] is not considered in our reconstruction. By knowing the phase in the photoelectron spectrum, together with the high-harmonic spectrum, we could reconstruct the temporal shape of the attosecond pulses. The reconstructed XUV pulse intensity is shown in Fig. 5(c). With the expected small femtochirp, there are five main attosecond bursts per pulse train, with an average burst duration of around 271 as.

The durations of the pump and probe pulses are monitored each day by RABBITT measurements. On average, one RABBITT measurement is performed per three transient absorption scans. The cross-correlation width (i.e., the correlation of the pump and probe pulses) is extracted from fits to the measured RABBITT sidebands with an oscillating function $f(\tau)$:

$$f(\tau) = \exp\left(-\left(\frac{(\tau - t_0)}{e}\right)^2\right) * (a * \sin(\omega_0\tau + b) + c) + d, \tag{C1}$$

where the center wavelength $\omega_0$ is kept fixed for all fits. Figure 6(b) shows the cross-correlation width of the

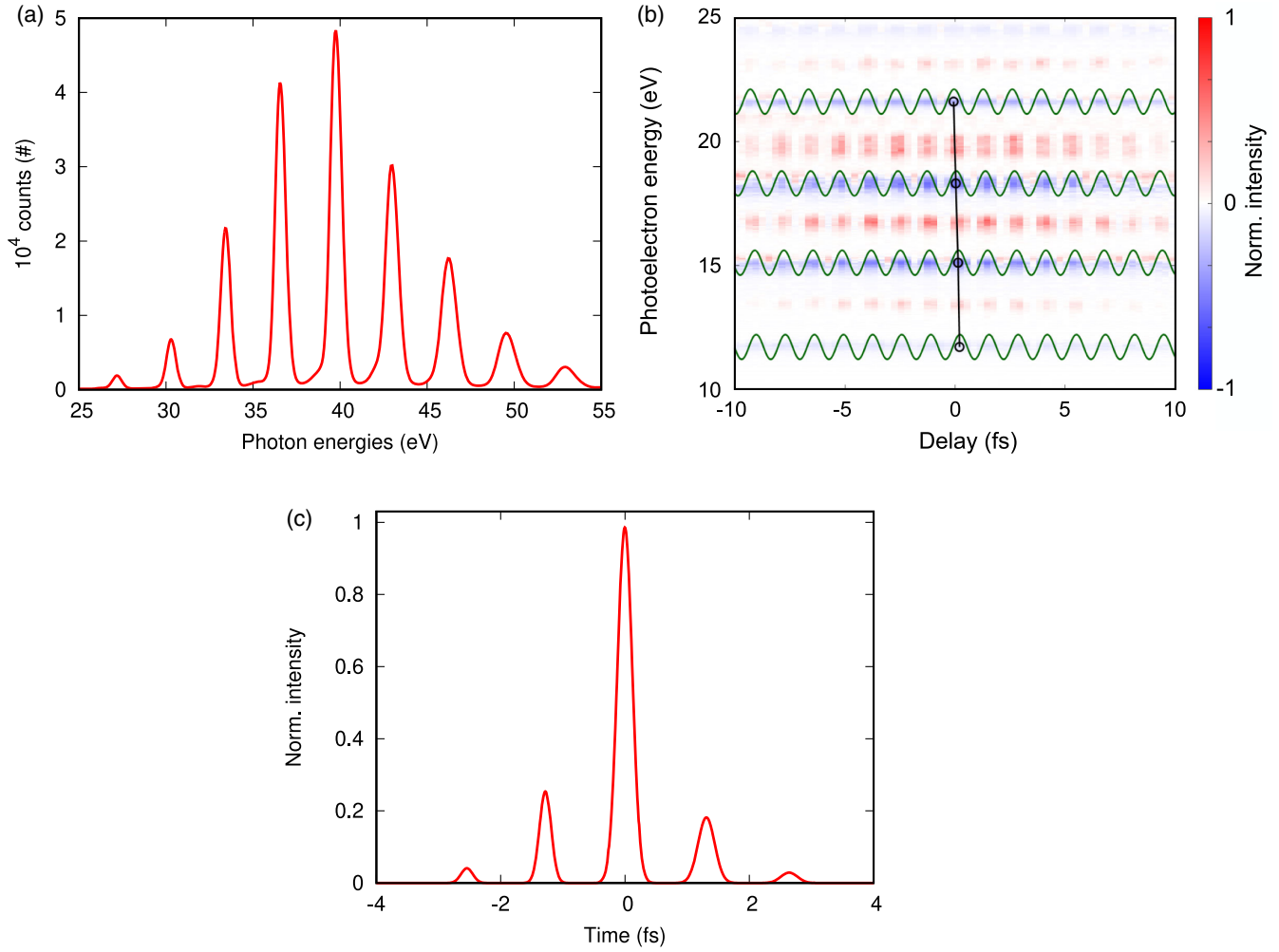


FIG. 5. (a) XUV spectrum. (b) Differential RABBITT spectrogram. The photoelectron spectrum is recorded as a function of pump-probe delay, where positive delays mean that the infrared pulse arrives before the XUV pulse. (c) Reconstructed XUV intensity.

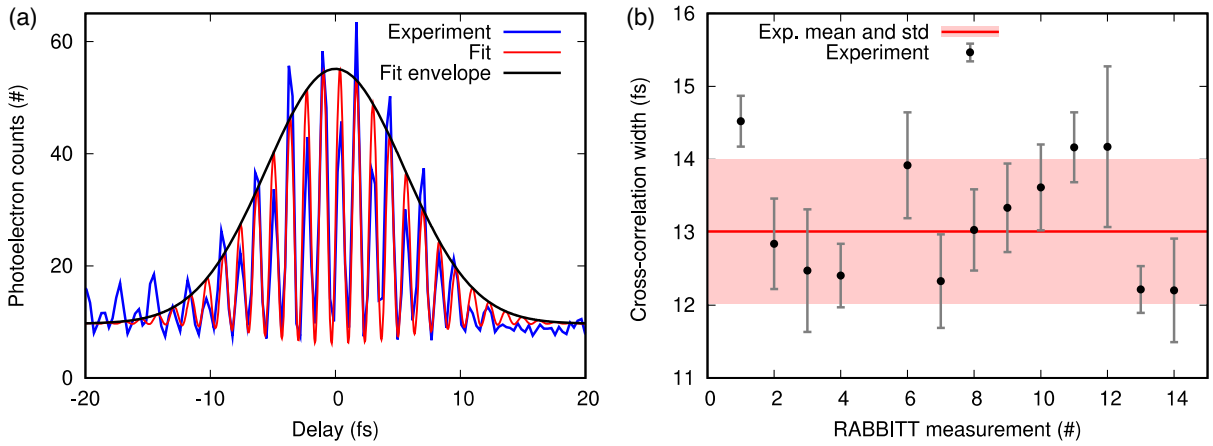


FIG. 6. (a) Fit of sideband oscillations from a RABBITT measurement. From the FWHM of the fit, the cross-correlation width is determined. The blue line shows the measured oscillations of an individual sideband of a RABBITT measurement, the red line shows the fitted function, and the black line shows the fitted Gaussian envelope. (b) Cross-correlation widths and their standard errors from the individual RABBITT measurements. The average cross-correlation width (red line) and its standard deviation (red area) are $13 \pm 1$ fs.

different RABBITT measurements, which yields, on average, $13 \pm 1$ fs.

## APPENDIX D: STATISTICAL ROBUSTNESS

To obtain statistically robust data, we take in total 45 measurements performed over 7 different days. Each measurement takes around 1 h. After each measurement, the spatial pump-probe overlap is checked, and a RABBITT measurement is performed to find the pump-probe delay of zero. Figure 7 shows one randomly selected data set for each day of measurement and the weighted average over all 45 measurements. We apply weighted averaging (see Appendix B); thus, the best-quality data sets receive the most weight. The qualitative trend of the change in optical density with delay is already visible in the individual measurements, with considerably larger signal fluctuations due to noise, however.

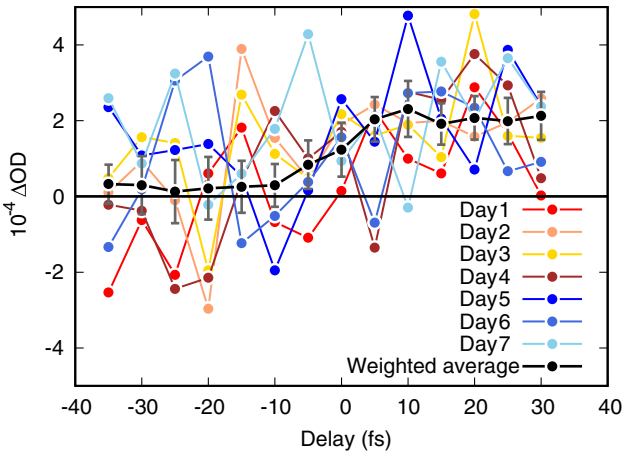


FIG. 7. Individual optical density measurements (colored lines) at the photon energy of 38.7–40.7 eV acquired on different days, compared to the weighted average [black dots; see Eq. (B2)] of all 45 measurements. The gray markers correspond to the standard error. Overall, the individual measurements show the same trend as their weighted average with much bigger fluctuations.

Additionally, measurements with a delay step size of 250 as are performed, and no evidence for field-driven $2\omega$ dynamics within a sensitivity of about $4 \times 10^{-3}$ OD is found (see Fig. 8).

## APPENDIX E: RESPONSE TIME

Figure 9 shows the transient signals evaluated in different photon energy intervals. Each signal is fitted with a sigmoid function [Eq. (E1)]. The characteristic time and the amplitude of the best-fit sigmoid function are shown in Table I.

$$f(t) = \frac{a}{1 + \exp(-\frac{t-t_0}{\tau})} + a_0. \tag{E1}$$

This analysis shows that the dynamics in the free-free absorption range of aluminum does not exhibit a significant dependence on the photon energy in the investigated spectral range on the fs timescale. We observe a signal at negative time delays due to heating of the sample from previous laser pulses. This background signal is constant on a few-fs timescale and, thus, does not change the results of the nonequilibrium dynamics.

For the ps response (see Fig. 10), we observe an exponential increase in absorption for different energy windows. Each signal is fitted with an exponential function [Eq. (E2)]. The time constants on the ps scale agree within their error bars and are energy independent in the measured XUV range. This facilitates differentiating the lattice response from the electronic response. The characteristic time $b$ of the exponential fit function [Eq. (E2)] is shown in Table II

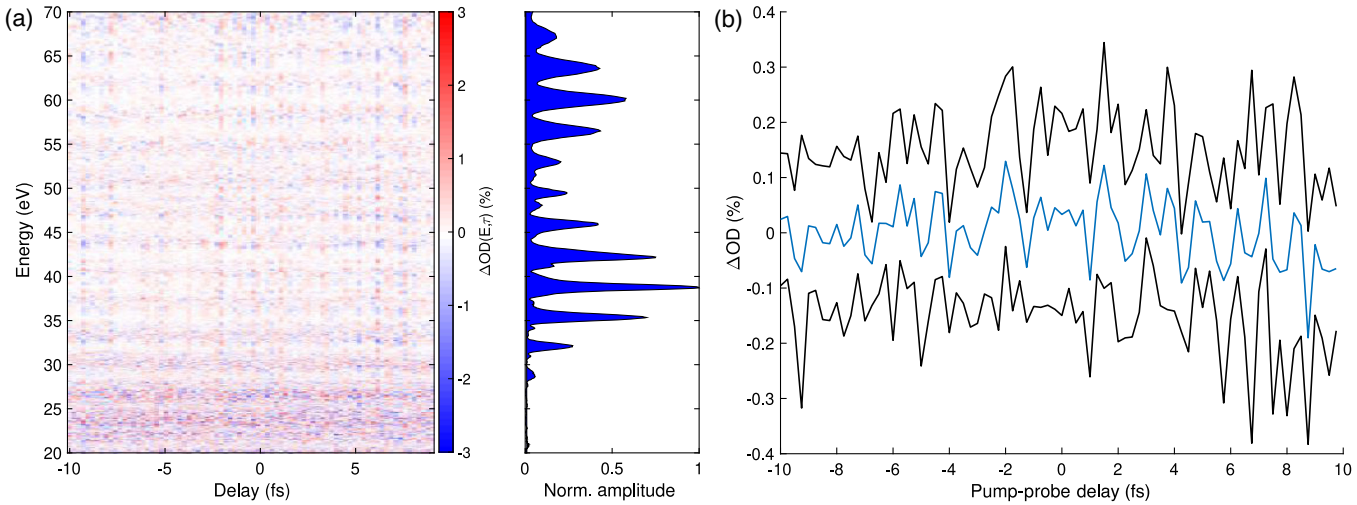


FIG. 8. (a) Transient absorption scan over 20 fs with a delay step size of 250 as. In panel (b), the blue line indicates the integrated change in optical density from 42 eV to 44 eV, while the black lines show the standard error. There is no evidence for field-driven $2\omega$ dynamics within a sensitivity $\Delta\mathrm{OD} \approx 4 \times 10^{-3}$.

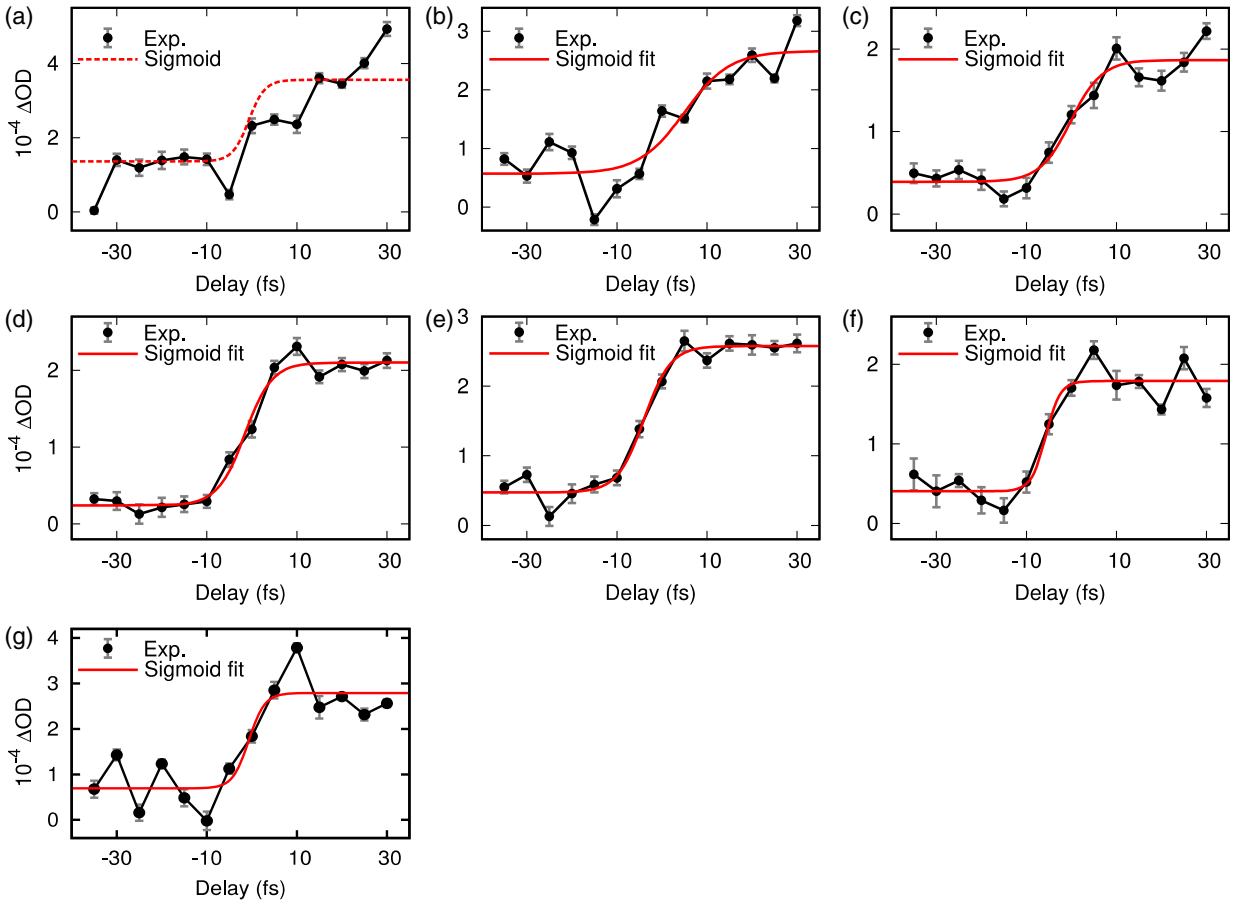


FIG. 9. Sigmoid fits (red lines) of the transient absorption scans for different energy regions on the fs timescale. The sigmoid in panel (a) is not a fit but a guide to the eye. The black points and the gray markers correspond to the measured change in optical density and to their standard error, respectively. The labels (b) to (g) correspond to different energy regions which are indicated in Table I. The energy region of panel (a) lies between 30 eV and 30.5 eV.

TABLE I. Fitting values of the sigmoid function to the individual optical density changes on the fs timescale.

| Panel | Energy region (eV) | Characteristic time (fs) | Amplitude |
|---|---|---|---|
| (b) | 33.5–33.8 | $22 \pm 14$ | $2.1 \pm 0.4$ |
| (c) | 35.5–37.5 | $15 \pm 6$ | $1.5 \pm 0.1$ |
| (d) | 38.7–40.7 | $13 \pm 3$ | $1.9 \pm 0.1$ |
| (e) | 42.0–44.0 | $13 \pm 3$ | $2.1 \pm 0.1$ |
| (f) | 45.6–46.1 | $7 \pm 6$ | $1.4 \pm 0.2$ |
| (g) | 49.5–50.0 | $8 \pm 10$ | $2.1 \pm 0.3$ |

$$f(t) = a(1 - \exp(-t/b)) + c. \tag{E2}$$

## APPENDIX F: FIRST-PRINCIPLES ELECTRON DYNAMICS SIMULATION AND OPTICAL PROPERTIES OF SOLIDS

To investigate the optical properties of laser-excited aluminum, we employ the real-time electron dynamics simulation based on the time-dependent density functional theory [31,32]. The real-time method is an efficient approach to study optical properties in high-energy regions because it directly evolves quantum states without explicit use of unoccupied states. We briefly describe the methods below, while the theoretical methods were described in detail elsewhere [33]. The electron dynamics in solids is calculated with the following time-dependent Kohn-Sham equation:

TABLE II. Fitting values of the exponential function to the individual optical density changes on the ps timescale.

| Panel | Energy region (eV) | Characteristic time (fs) |
|---|---|---|
| (a) | 29.6–30.6 | $251 \pm 71$ |
| (b) | 32.8–33.8 | $323 \pm 67$ |
| (c) | 35.3–37.3 | $319 \pm 61$ |
| (d) | 38.5–40.5 | $253 \pm 50$ |
| (e) | 42.3–43.3 | $274 \pm 62$ |

$$i\hbar \frac{\partial}{\partial t} u_{bk}(\boldsymbol{r}, t) = \left[ \frac{1}{2} \left( \boldsymbol{p} + \hbar \boldsymbol{k} + \frac{1}{c} \boldsymbol{A}(t) \right)^2 + \hat{v}_{\mathrm{ion}} + v_{\mathrm{Hxc}}(\boldsymbol{r}, t) \right] u_{bk}(\boldsymbol{r}, t), \tag{F1}$$

where $b$ is the band index, $\boldsymbol{k}$ is the Bloch wave vector, and $u_{bk}(\boldsymbol{r}, t)$ is the periodic part of the Bloch wave function. The ionic potential is denoted as $\hat{v}_{\mathrm{ion}}$, and the Hartree-exchange-correlation potential is denoted as $v_{\mathrm{Hxc}}(\boldsymbol{r}, t)$. In the present work, we employ the norm-conserving pseudopotential for the ionic potential $\hat{v}_{\mathrm{ion}}$ [34]. The Hartree-exchange-correlation potential is evaluated with the electron density defined as $\rho(r, t) = \sum_{bk} f_{bk} |u_{bk}(\boldsymbol{r}, t)|^2$, where $f_{bk}$ is the occupation factor. The adiabatic local-density approximation [35] is used for the exchange-correlation potential. The applied laser field is described by the time-dependent vector potential $\boldsymbol{A}(t)$, which is related to the external electric field as $\boldsymbol{A}(t) = -c \int^t dt' \boldsymbol{E}(t)$. In this work, we employ a

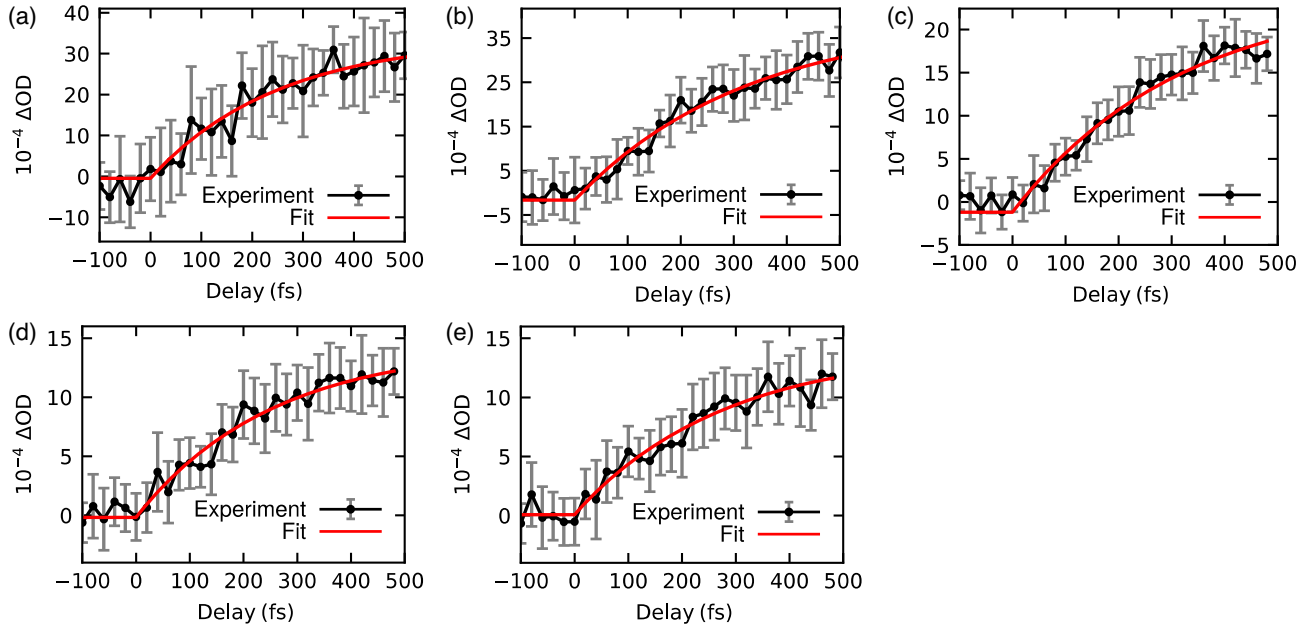


FIG. 10. Exponential fits (red lines) of the transient absorption scans for different energy regions on the ps timescale. The black points and the gray markers correspond to the measured change in optical density and to their standard error, respectively. The labels (a) to (e) correspond to different energy regions as indicated in Table II.

weak impulsive distortion as the applied electric field, $\boldsymbol{E}(t) = \boldsymbol{e}_x E_0 \delta(t)$. All the simulations in the present work were performed with the Octopus code [36]. The primitive cell of the aluminum was discretized into 203 real-space grid points, and the first Brillouin zone was discretized into 523 k-grid points. We have confirmed the numerical convergence of the following optical response for the chosen number of real-space grid points and the Brillouin zone sampling (k-points). Note that, in the present work, the ionic positions are frozen at their equilibrium position.

Employing the time-evolving wave function, the electric current can be evaluated as

$$J(t) = -\frac{1}{\Omega}\sum_{b\boldsymbol{k}} f_{b\boldsymbol{k}} \int_{\Omega} d\boldsymbol{r} u^*_{b\boldsymbol{k}}(\boldsymbol{r},t)\left(\boldsymbol{p} + \hbar\boldsymbol{k} + \frac{1}{c}\boldsymbol{A}(t) + \frac{[r, \hat{v}_{\mathrm{ion}}]}{i\hbar}\right) u_{b\boldsymbol{k}}(\boldsymbol{r},t), \tag{F2}$$

where $\Omega$ is the volume of the unit cell. Furthermore, the diagonal part of the optical conductivity can be evaluated as

$$\sigma(\omega) = \frac{\int dt e^{i\omega t-\gamma t}\boldsymbol{e}_x \cdot \boldsymbol{J}(t)}{\int dt e^{i\omega t-\gamma t}\boldsymbol{e}_x \cdot \boldsymbol{E}(t)} = \frac{1}{E_0}\int dt e^{i\omega t-\gamma t} J_x(t), \tag{F3}$$

where $\gamma$ is the phenomenological damping rate. One can further evaluate the dielectric function $\epsilon(\omega)$ and the absorption coefficient $\mu(\omega)$ as

$$\epsilon(\omega) = 1 + \frac{4\pi i}{\omega}\sigma(\omega), \tag{F4}$$

$$\mu(\omega) = \frac{2\omega}{c}\Im[\sqrt{\epsilon(\omega)}]. \tag{F5}$$

Note that the results with different damping rates are shown in Fig. 1(a) in the main text.

## APPENDIX G: THEORETICAL EVALUATION OF THE OPTICAL DENSITY OF THE LASER-EXCITED ALUMINUM THIN FILM

We theoretically model the optical property of laser-excited aluminum with the finite electron-temperature TDDFT calculation [37]. Here, the dielectric function of the laser-excited system is evaluated with the above TDDFT calculation, but the occupation factor $f_{b\boldsymbol{k}}$ is given by the Fermi-Dirac distribution with the finite electron temperature $T_e$, assuming that the laser-excited system is well characterized by a hot-electron state. Hence, the dielectric function is also a function of the electron temperature as $\epsilon(\omega, T_e)$. Note that the excess energy due to the electron temperature increase can also be evaluated with the finite electron-temperature DFT calculation. For later convenience, we define the excess energy as the total energy increase from room temperature as

$$\Delta E_{\mathrm{excess}}(T_e) = E_{\mathrm{total}}(T_e) - E_{\mathrm{total}}(T_e = 300\ \mathrm{K}). \tag{G1}$$

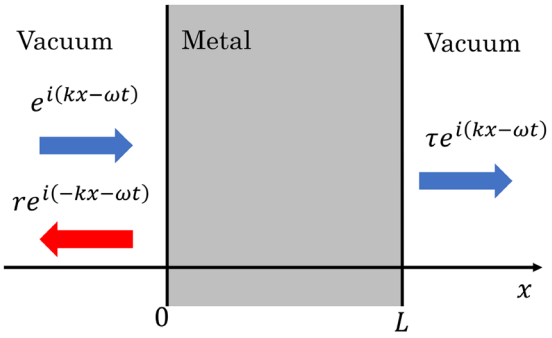


FIG. 11. Schematic of laser-field irradiation of aluminum thin film.

It should be noted that the NIR pump pulse nonuniformly excites electrons inside the thin film because the NIR pulse is strongly absorbed near the front surface and it does not reach the rear surface. To take into account this nonuniform excitation effect, we first estimate the distribution of the energy deposition of the NIR field.

For this purpose, we consider a stationary solution of the Maxwell equation in the one-dimensional geometry shown in Fig. 11. In the region $x < 0$, the electric field $E(x<0,t)$ is the sum of the incident field $e^{i(kx-\omega t)}$ and the reflected field $re^{i(-kx-\omega t)}$, with the reflection coefficient $r$ as $E(x<0,t) = e^{i(kx-\omega t)} + re^{i(-kx-\omega t)}$. In the region $x > L$, the transmitted field in vacuum is described as a plane wave, $E(x>L,t) = \tau e^{i(kx-\omega t)}$, with the transmission coefficient $\tau$. Inside the thin film, the electric field satisfies the following wave equation,

$$\left[\frac{\partial^2}{\partial x^2} + \frac{\omega^2}{c^2}\epsilon(x,\omega)\right]E(x,t) = 0, \tag{G2}$$

where $\epsilon(x,\omega)$ is the dielectric function. For later convenience, we keep the spatial dependence of the dielectric function inside the thin film. Imposing the continuity of the electric field and its first derivative in the whole space, one can solve the above wave equation and obtain the reflection and transmission coefficients, $r$ and $\tau$.

To estimate the deposited energy distribution by the NIR pulse, we solve the above wave equation by setting $\omega$ to 1.6 eV/$\hbar$ and $\epsilon(x, \omega = 1.6\ \mathrm{eV}/\hbar)$ to $-66.405 + i44.255$ according to experimental data from the literature [38]. Assuming linear absorption of the NIR pulse, the deposited energy distribution is proportional to the square of the field strength, $\Delta E_{\mathrm{excess}}(x) = \alpha|E(x,t)|^2$, where $\alpha$ is a scaling factor. Once the deposited energy is evaluated, one can further estimate the local electron temperature as a function

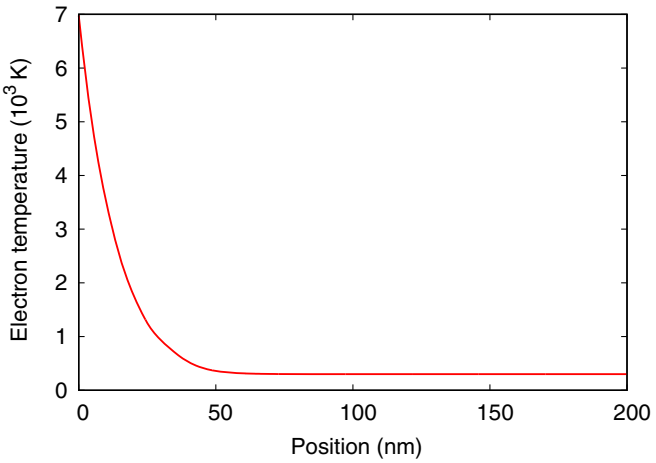


FIG. 12. Electron-temperature distribution in bulk aluminum as a function of the position from the surface.

of depth via Eq. (G1). Furthermore, the spatial dependence of the dielectric function in Eq. (G2) can be evaluated via the spatial dependence of the electron temperature.

By solving the wave equation, Eq. (G2), with the spatially dependent dielectric function, one can further evaluate the transmittivity $|\tau|^2$ and optical density $-\ln|\tau|^2$ while considering the effects of the nonuniform laser excitation inside the thin film.

Figure 12 shows the obtained electron-temperature distribution. Here, we choose the scaling constant $\alpha$ for the deposited energy distribution $\Delta E_{\mathrm{excess}}(x) = \alpha|E(x,t)|^2$ so that the evaluated $\Delta$OD reproduces the experimental observation. As seen from Fig. 12, the electrons are heated up to a peak temperature of 7000 K at the surface, with a rapid decrease in temperature with penetration depth in accordance with the optical attenuation of the pump pulse. Note that 7000 K corresponds to an excess energy of 0.24 eV/atom, well below the cohesive energy of aluminum, which is 3.39 eV/atom [39].

## APPENDIX H: PROPAGATION EFFECT AND ABSORPTION

With the above analysis based on Eq. (G2), we investigate the transmission and optical density with the full solution of Maxwell's equation. Therefore, the propagation effects such as reflection are fully included. Here, to assess the absorption contribution, we evaluate the transmission based on the Beer-Lambert law. Based on the electron-temperature distribution shown in Fig. 12, we first evaluate the absorption coefficient with Eq. (F5) as a function of depth, $\mu(x)$. Then, the transmittivity is evaluated by

$$T_{\mathrm{abs}} = \exp\left[-\int_0^L dx\,\mu(x)\right]. \tag{H1}$$

## APPENDIX I: ASSESSMENT OF MANY-BODY EFFECTS WITH THE INDEPENDENT PARTICLE APPROXIMATION

In the above analysis, we evaluated the optical property of aluminum with the finite electron-temperature TDDFT calculation. To assess the role of dynamical many-body effects, we repeat the analysis by employing an IP calculation that ignores such effects. For this purpose, we freeze the Hartree-exchange-correlation potential to that of the ground state at room temperature, $T_e = 300$ K. As a result, the time and temperature dependence of $v_{\mathrm{Hxc}}(\boldsymbol{r},t)$ are completely ignored. The electron temperature affects only the occupation factors $f_{b\boldsymbol{k}}$ in the current evaluation with Eq. (F2). Figure 2(b) in the main text shows the comparison of the full TDDFT calculation and this independent particle calculation, demonstrating that the many-body effects play no significant role. Hence, the observed modification of optical properties of aluminum is expected to be adequately explained in the independent particle picture. We would like to note that the change in absorption is unaffected by these inelastic many-body effects. The many-body effects enter the absorption coefficient via the broadening parameter of the TDDFT.

## APPENDIX J: NEARLY FREE ELECTRON MODEL

In order to provide microscopic insight into the phenomena, we investigate the change of the optical absorption of the metallic system due to the electron-temperature increase based on a nearly free electron model. For this purpose, we consider an electronic system described by the following Hamiltonian:

$$H = \frac{\boldsymbol{p}^2}{2m} + V(\boldsymbol{r}), \tag{J1}$$

where $V(\boldsymbol{r})$ is a periodic potential, $V(\boldsymbol{r}) = V(\boldsymbol{r}+\boldsymbol{a}_j)$, with the lattice vectors $\boldsymbol{a}_j$. Assuming that the potential $V(\boldsymbol{r})$ is weak, we analyze the following Schrödinger equation with perturbation theory,

$$H|\psi_{\boldsymbol{k}}\rangle = E_{\boldsymbol{k}}|\psi_{\boldsymbol{k}}\rangle. \tag{J2}$$

To evaluate the eigenstates $|\psi_{\boldsymbol{k}}\rangle$, we consider the following perturbative expansion up to the first order,

$$|\psi_{\boldsymbol{k}}\rangle \approx |\boldsymbol{k}\rangle + \sum_{\boldsymbol{G}\neq 0} c_{\boldsymbol{k}+\boldsymbol{G}}|\boldsymbol{k}+\boldsymbol{G}\rangle, \tag{J3}$$

where $|\boldsymbol{k}\rangle$ are plane-wave states, which are eigenstates of the unperturbed system, $\boldsymbol{G}$ are the reciprocal lattice vectors, and $c_{\boldsymbol{k}+\boldsymbol{G}}$ are the expansion coefficients. Inserting Eq. (J3) into Eq. (J2), one can evaluate the expansion coefficients as

$$c_{\boldsymbol{k}+\boldsymbol{G}} = -\frac{\langle \boldsymbol{k}+\boldsymbol{G}|V(\boldsymbol{r})|\boldsymbol{k}\rangle}{\epsilon_{\boldsymbol{k}+\boldsymbol{G}}-\epsilon_{\boldsymbol{k}}} = -\frac{\tilde{V}(-\boldsymbol{G})}{\epsilon_{\boldsymbol{k}+\boldsymbol{G}}-\epsilon_{\boldsymbol{k}}}, \tag{J4}$$

where $\epsilon_{\boldsymbol{k}}$ is the eigenenergy of the unperturbed system given by $\epsilon_{\boldsymbol{k}} = \boldsymbol{k}^2/2m$, and $\tilde{V}(-\boldsymbol{G})$ is the Fourier transform of the periodic potential $V(\boldsymbol{r})$.

Next, we investigate the optical absorption with the nearly free electron model. For this purpose, we calculate the real part of the optical conductivity as

$$\mathrm{Re}[\sigma(\omega, T_e)] = \frac{\pi}{\Omega}\sum_{\boldsymbol{G}}\int d\boldsymbol{k} n^F(\epsilon_{\boldsymbol{k}}, T_e)\frac{|\langle\psi_{\boldsymbol{k}+\boldsymbol{G}}|\boldsymbol{p}|\psi_{\boldsymbol{k}}\rangle|^2}{\epsilon_{\boldsymbol{k}+\boldsymbol{G}}-\epsilon_{\boldsymbol{k}}}\delta(\epsilon_{\boldsymbol{k}+\boldsymbol{G}}-\epsilon_{\boldsymbol{k}}-\omega), \tag{J5}$$

where $n^F(\epsilon, T_e)$ is the Fermi-Dirac distribution defined as

$$n^F(\epsilon, T_e) = \frac{1}{e^{(\epsilon-\mu)/k_B T_e}+1}. \tag{J6}$$

Here, we assume that the temperature is sufficiently low, and the occupations of the final states $|\psi_{\boldsymbol{k}}\rangle$ are completely zero.

Employing Eqs. (J3) and (J5), the real part of the conductivity can be rewritten as

$$\begin{aligned}\mathrm{Re}[\sigma(\omega, T_e)] &= \frac{\pi}{\Omega}\sum_{\boldsymbol{G}}\int d\boldsymbol{k} n^F(\epsilon_{\boldsymbol{k}}, T_e)\frac{G^2|\tilde{V}(\boldsymbol{G})|^2}{(\epsilon_{\boldsymbol{k}+\boldsymbol{G}}-\epsilon_{\boldsymbol{k}})^3}\delta(\epsilon_{\boldsymbol{k}+\boldsymbol{G}}-\epsilon_{\boldsymbol{k}}-\omega)\\ &= \frac{2\pi^3}{\Omega}\frac{m^2}{\omega^3}\sum_{\boldsymbol{G}}G|\tilde{V}(\boldsymbol{G})|^2\int_0^\infty d\epsilon_k n^F(\epsilon_k, T_e)\Theta\left(\frac{Gk}{m}-\left|\frac{G^2}{2m}-\omega\right|\right),\end{aligned} \tag{J7}$$

where $\Theta(x)$ is the Heaviside step function.

Then, we investigate the temperature dependence of the optical absorption of the nearly free electron model. For this purpose, we consider the Sommerfeld expansion of an observable in the low-temperature limit as

$$\tilde{A}(T_e) = \int_{-\infty}^{\infty} d\epsilon n^F(\epsilon, T_e)A(\epsilon) \approx \int_{-\infty}^{\epsilon_F} d\epsilon A(\epsilon) + \int_{\epsilon_F}^{\mu} d\epsilon A(\epsilon) + \frac{\pi^2}{6}(k_B T_e)^2\left.\frac{dA}{d\epsilon}\right|_{\epsilon=\epsilon_F}, \tag{J8}$$

where $A(\epsilon)$ is the observable depending on the energy of the states $\epsilon$. On the right-hand side of the equation, the second term originates from the chemical potential shift by the temperature increase, while the third term originates from the smearing of the Fermi-Dirac distribution. By considering the chemical potential shift of the three-dimensional Fermi gas, $\mu = \epsilon_F - \pi^2(k_B T_e)^2/12\epsilon_F$, one can obtain the following expression,

$$\tilde{A}(T_e) \approx \int_{-\infty}^{\epsilon_F} d\epsilon A(\epsilon) - \frac{\pi^2}{12}(k_B T_e)^2 A(\epsilon_F) + \frac{\pi^2}{6}(k_B T_e)^2\left.\frac{dA}{d\epsilon}\right|_{\epsilon=\epsilon_F}. \tag{J9}$$

Importantly, by applying the expansion of Eq. (J9) to Eq. (J7), the chemical potential shift decreases the photo-absorption with the increase in the electron temperature, while the smearing of the Fermi-Dirac distribution increases the absorption.

Employing Eq. (J9), the change of the real part of the conductivity can be described as

$$\mathrm{Re}[\sigma(\omega, T_e)] - \mathrm{Re}[\sigma(\omega, 0)] = T_e^2\frac{k_B^2\pi^2}{6}\frac{2\pi^2}{\Omega}\frac{m^2}{k_F}\sum_{\boldsymbol{G}}G^2|\tilde{V}(\boldsymbol{G})|^2 S_G(\omega), \tag{J10}$$

where $k_F$ is the Fermi wavenumber, $k_F = \sqrt{2m\epsilon_F}$, and $S_G(\omega)$ is a function of frequency defined by

$$S_G(\omega) = \frac{1}{\omega^3}\left[\delta\left(\omega-\frac{G^2}{2m}-\frac{Gk_F}{m}\right)+\delta\left(\omega-\frac{G^2}{2m}+\frac{Gk_F}{m}\right)-\frac{m}{Gk_F}\Theta\left(\frac{Gk_F}{m}-\left|\frac{G^2}{2m}-\omega\right|^2\right)\right]. \tag{J11}$$

To elucidate a contribution from each final state $|\boldsymbol{k}+\boldsymbol{G}\rangle$ to the change of the absorption, we evaluate the following spectral weight:

$$W_G = \int_0^\infty d\omega S_G(\omega) = \left(\frac{2m}{G^2}\right)^3 \frac{8(\frac{2k_F}{G})^2}{(1-(\frac{2k_F}{G})^2)^3}. \quad \text{(J2)}$$

Here, the spectral weight $W_G > 0$ for $G > 2k_F$, while $W_G < 0$ for $G < 2k_F$. Therefore, if $|\boldsymbol{G}| > 2k_F$, the transition from $|\psi_{\boldsymbol{k}}\rangle$ to $|\psi_{\boldsymbol{k}+\boldsymbol{G}}\rangle$ has a positive contribution to the change of the optical absorption with increasing temperature. On the other hand, if $|\boldsymbol{G}| < 2k_F$, the transition from $|\psi_{\boldsymbol{k}}\rangle$ to $|\psi_{\boldsymbol{k}+\boldsymbol{G}}\rangle$ has a negative contribution. Since a large value of $|\boldsymbol{G}|$ corresponds to the absorption of higher-energy photons, Eq. (J12) indicates that a simple metal shows an increase in photoabsorption in the higher-energy region with increasing temperature, while it shows a decrease in the lower-energy region. This finding is consistent with the observations in both experiments and first-principles simulations.

## APPENDIX K: IMPACT OF THE ELECTRON-TEMPERATURE CHANGE ON THE ELECTRON-PHONON SCATTERING RATE

Here, we estimate the effect of electron-temperature change on the electron-phonon scattering rate. The electron-phonon scattering rate of electrons at a Bloch state $|u_{n\boldsymbol{k}}\rangle$ can be described as [40,41]

$$\Gamma_{n\boldsymbol{k}} = \frac{2\pi}{\hbar}\sum_{m\boldsymbol{q}\nu}|g_{nm,\nu(\boldsymbol{k},\boldsymbol{q})}|^2(1-\cos\theta_{\boldsymbol{k},\boldsymbol{k}+\boldsymbol{q}})[(N_{\nu\boldsymbol{q}}+f_{m\boldsymbol{k}+\boldsymbol{q}})\delta(\epsilon_{n\boldsymbol{k}+\hbar\omega_{\nu\boldsymbol{q}}}-\epsilon_{m\boldsymbol{k}+\boldsymbol{q}})+(N_{\nu\boldsymbol{q}}+1-f_{m\boldsymbol{k}+\boldsymbol{q}})\delta(\epsilon_{n\boldsymbol{k}}-\hbar\omega_{\nu\boldsymbol{q}}-\epsilon_{m\boldsymbol{k}+\boldsymbol{q}})], \quad \text{(K1)}$$

where $g_{nm,\nu(\boldsymbol{k},\boldsymbol{q})}$ are electron-phonon coupling matrix elements between the initial Bloch state $|u_{n\boldsymbol{k}}\rangle$ and the final Bloch state $|u_{m\boldsymbol{k}+\boldsymbol{q}}\rangle$ via a phonon mode $\nu$ with wave vector $\boldsymbol{q}$ and frequency $\omega_{\nu\boldsymbol{q}}$. Here, $\epsilon_{m\boldsymbol{k}}$ are single-particle energies of Bloch states $|u_{m\boldsymbol{k}}\rangle$, and $f_{m\boldsymbol{k}}$ are the occupations of those states. The phonon occupations are denoted as $N_{\nu\boldsymbol{q}}$. Since we investigate photoabsorption in the XUV regime, we consider the electron-phonon scattering rate $\Gamma_{n\boldsymbol{k}}$ for high-energy electrons: The energy of the final states $|u_{m\boldsymbol{k}+\boldsymbol{q}}\rangle$ from the Fermi surface, $\epsilon_{m\boldsymbol{k}+\boldsymbol{q}}-\epsilon_F$, is on the order of a few tens of eV. In this regime, the occupations of the final states, $f_{m\boldsymbol{k}+\boldsymbol{q}}$, are almost zero since the electron temperature is at most on the order of eV even after the photoexcitation. Therefore, the above scattering rate for high-energy electrons can be approximated as

$$\Gamma_{n\boldsymbol{k}} \approx \frac{2\pi}{\hbar}\sum_{m\boldsymbol{q}\nu}|g_{nm,\nu(\boldsymbol{k},\boldsymbol{q})}|^2(1-\cos\theta_{\boldsymbol{k},\boldsymbol{k}+\boldsymbol{q}})[N_{\nu\boldsymbol{q}}\delta(\epsilon_{n\boldsymbol{k}+\hbar\omega_{\nu\boldsymbol{q}}}-\epsilon_{m\boldsymbol{k}+\boldsymbol{q}})+(N_{\nu\boldsymbol{q}}+1)\delta(\epsilon_{n\boldsymbol{k}}-\hbar\omega_{\nu\boldsymbol{q}}-\epsilon_{m\boldsymbol{k}+\boldsymbol{q}})]. \quad \text{(K2)}$$

Hence, for high-energy electrons ($\epsilon_{n\boldsymbol{k}}-\epsilon_F \gg k_B T_e$), the electron-phonon scattering rate is independent from the electron temperature and occupation.

## APPENDIX L: INTERBAND MODEL

For a given photon energy, the interband transition rate is proportional to the product of filled initial states and empty final states, that is, the joint density of states:

$$\mathrm{JDOS}(\hbar\omega,\mathrm{T}) = \frac{1}{2\pi^2}\left(\frac{2\mu}{\hbar^2}\right)^{\frac{3}{2}}\int_{E=0}^{E=\infty} dE\sqrt{E}n(E,T)\times\sqrt{E+\hbar\omega}(1-n(E+\hbar\omega,T)). \quad \text{(L1)}$$

Here, the density of states is given by the 3D free-electron gas expression and is proportional to $\sqrt{\mathrm{E}}$, and the occupation is given by the Fermi-Dirac distribution $n$, with the temperature-dependent chemical potential $\mu(T)$, and $\hbar\omega$ corresponds to the XUV probe transitions. The resultant change in absorption between $T_1 = 300$ K and $T_2 = 7000$ K is shown in Fig. 3(b) by the solid black curve. We see that this model with a temperature-dependent chemical potential is able to reproduce the TDDFT results. The difference of the fine structures above the plasma frequency at 16 eV results from the deviations of the band structure of aluminum from the band structure of a quasi-free electron gas.

[1] J. Meyer-Ter-Vehn and R. Ramis, *On Collisional Free-Free Photon Absorption in Warm Dense Matter*, Phys. Plasmas **26**, 113301 (2019).

[2] S. Vago and S. Hocini, *Electromagnetic Radiation in Non-Thermal Quantum Plasmas*, J. Phys. A **21**, 3763 (1988).

[3] M. Schultze, E. M. Bothschafter, A. Sommer, S. Holzner, W. Schweinberger, M. Fiess, M. Hofstetter, R. Kienberger, V. Apalkov, V. S. Yakovlev, M. I. Stockman, and F. Krausz, *Controlling Dielectrics with the Electric Field of Light.*, Nature (London) **493**, 75 (2013).

[4] M. Lucchini, S. A. Sato, A. Ludwig, J. Herrmann, M. Volkov, L. Kasmi, Y. Shinohara, K. Yabana, L. Gallmann, and U. Keller, *Attosecond Dynamical Franz-Keldysh Effect in Polycrystalline Diamond*, Science **353**, 916 (2016).

[5] F. Schlaepfer, M. Lucchini, S. A. Sato, M. Volkov, L. Kasmi, N. Hartmann, A. Rubio, L. Gallmann, and U. Keller, *Attosecond Optical-Field-Enhanced Carrier Injection into the GaAs Conduction Band*, Nat. Phys. **14**, 560 (2018).

[6] M. Volkov, S. A. Sato, F. Schlaepfer, L. Kasmi, N. Hartmann, M. Lucchini, L. Gallmann, A. Rubio, and U. Keller, *Attosecond Screening Dynamics Mediated by Electron Localization in Transition Metals*, Nat. Phys. **15**, 1145 (2019).

[7] G. O. Williams *et al.*, *Tracking the Ultrafast XUV Optical Properties of X-Ray Free-Electron-Laser Heated Matter with High-Order Harmonics*, Phys. Rev. A **97**, 023414 (2018).

[8] N. R. Shaffer, N. G. Ferris, J. Colgan, D. P. Kilcrease, and C. E. Starrett, *Free-Free Opacity in Dense Plasmas with an Average Atom Model*, High Energy Density Phys. **23**, 31 (2017).

[9] S. M. Vinko, G. Gregori, M. P. Desjarlais, B. Nagler, T. J. Whitcher, R. W. Lee, P. Audebert, and J. S. Wark, *Free-Free Opacity in Warm Dense Aluminum*, High Energy Density Phys. **5**, 124 (2009).

[10] S. Ichimaru, *Strongly Coupled Plasmas: High-Density Classical Plasmas and Degenerate Electron Liquids*, Rev. Mod. Phys. **54**, 1017 (1982).

[11] F. C. Kabeer, E. S. Zijlstra, and M. E. Garcia, *Road of Warm Dense Noble Metals to the Plasma State: Ab Initio Theory of the Ultrafast Structural Dynamics in Warm Dense Matter*, Phys. Rev. B **89**, 100301 (2014).

[12] C. A. Iglesias, *XUV Absorption by Solid-Density Aluminum*, High Energy Density Phys. **6**, 311 (2010).

[13] P. Hollebon, O. Ciricosta, M. P. Desjarlais, C. Cacho, C. Spindloe, E. Springate, I. C. E. Turcu, J. S. Wark, and S. M. Vinko, *Ab Initio Simulations and Measurements of the Free-Free Opacity in Aluminum*, Phys. Rev. E **100**, 043207 (2019).

[14] D. Semkat, R. Redmer, and T. Bornath, *Collisional Absorption in Aluminum*, Phys. Rev. E **73**, 066406 (2006).

[15] B. Kettle, T. Dzelzainis, S. White, L. Li, B. Dromey, M. Zepf, C. L. S. Lewis, G. Williams, S. Künzel, M. Fajardo, H. Dacasa, P. Zeitoun, A. Rigby, G. Gregori, C. Spindloe, R. Heathcote, and D. Riley, *Experimental Measurements of the Collisional Absorption of XUV Radiation in Warm Dense Aluminium*, Phys. Rev. E **94**, 023203 (2016).

[16] S. M. Vinko *et al.*, *Time-Resolved XUV Opacity Measurements of Warm Dense Aluminum*, Phys. Rev. Lett. **124**, 225002 (2020).

[17] R. Locher, M. Lucchini, J. Herrmann, M. Sabbar, M. Weger, A. Ludwig, L. Castiglioni, M. Greif, M. Hengsberger, L. Gallmann, and U. Keller, *Versatile Attosecond Beamline in a Two-Foci Configuration for Simultaneous Time-Resolved Measurements*, Rev. Sci. Instrum. **85**, 013113 (2014).

[18] M. E. Povarnitsyn, D. V. Knyazev, and P. R. Levashov, *Ab Initio Simulation of Complex Dielectric Function for Dense Aluminum Plasma*, Contrib. Plasma Phys. **52**, 145 (2012).

[19] H. G. Muller, *Reconstruction of Attosecond Harmonic Beating by Interference of Two-Photon Transitions*, Appl. Phys. B **74**, s17 (2002).

[20] P. M. Paul, E. S. Toma, P. Breger, G. Mullot, F. Augé, P. Balcou, H. G. Muller, and P. Agostini, *Observation of a Train of Attosecond Pulses from High Harmonic Generation*, Science **292**, 1689 (2001).

[21] L. Waldecker, R. Bertoni, R. Ernstorfer, and J. Vorberger, *Electron-Phonon Coupling and Energy Flow in a Simple Metal beyond the Two-Temperature Approximation*, Phys. Rev. X **6**, 021003 (2016).

[22] B. Y. Mueller and B. Rethfeld, *Relaxation Dynamics in Laser-Excited Metals under Nonequilibrium Conditions*, Phys. Rev. B **87**, 035139 (2013).

[23] P. N. H. Nakashima, A. E. Smith, J. Etheridge, and B. C. Muddle, *The Bonding Electron Density in Aluminum*, Science **331**, 1583 (2011).

[24] J. Jiang, K. Shimada, H. Hayashi, H. Iwasawa, Y. Aiura, H. Namatame, and M. Taniguchi, *Coupling Parameters of Many-Body Interactions for the Al(100) Surface State: A High-Resolution Angle-Resolved Photoemission Spectroscopy Study*, Phys. Rev. B **84**, 155124 (2011).

[25] H. Ehrenreich, H. R. Philipp, and B. Segall, *Optical Properties of Aluminum*, Phys. Rev. **132**, 1918 (1963).

[26] Y. Takada and H. Yasuhara, *Dynamical Structure Factor of the Homogeneous Electron Liquid: Its Accurate Shape and the Interpretation of Experiments on Aluminum*, Phys. Rev. Lett. **89**, 216402 (2002).

[27] S. P. Singhal and J. Callaway, *Self-Consistent Energy Bands in Aluminum: An Improved Calculation*, Phys. Rev. B **16**, 1744 (1977).

[28] M. Zürch, H.-T. Chang, L. J. Borja, P. M. Kraus, S. K. Cushing, A. Gandman, C. J. Kaplan, M. H. Oh, J. S. Prell, D. Prendergast, C. D. Pemmaraju, D. M. Neumark, and S. R. Leone, *Direct and Simultaneous Observation of Ultrafast Electron and Hole Dynamics in Germanium*, Nat. Commun. **8**, 15734 (2017).

[29] S. K. Cushing, A. Lee, I. J. Porter, L. M. Carneiro, H.-T. Chang, M. Zürch, and S. R. Leone, *Differentiating Photoexcited Carrier and Phonon Dynamics in the Δ, L, and Γ Valleys of Si(100) with Transient Extreme Ultraviolet Spectroscopy*, J. Phys. Chem. C **123**, 3343 (2019).

[30] K. Varjú, Y. Mairesse, B. Carré, M. B. Gaarde, P. Johnsson, S. Kazamias, R. López-Martens, J. Mauritsson, K. J. Schafer, P. Balcou, A. L'Huillier, and P. Salières, *Frequency Chirp of Harmonic and Attosecond Pulses*, J. Mod. Opt. **52**, 379 (2005).

[31] E. Runge and E. K. U. Gross, *Density-Functional Theory for Time-Dependent Systems*, Phys. Rev. Lett. **52**, 997 (1984).

[32] G. F. Bertsch, J. I. Iwata, A. Rubio, and K. Yabana, *Real-Space, Real-Time Method for the Dielectric Function*, Phys. Rev. B **62**, 7998 (2000).

[33] S. A. Sato, *First-Principles Calculations for Attosecond Electron Dynamics in Solids*, Comput. Mater. Sci. **194**, 110274 (2021).

[34] C. Hartwigsen, S. Goedecker, and J. Hutter, *Relativistic Separable Dual-Space Gaussian Pseudopotentials from H to Rn*, Phys. Rev. B **58**, 3641 (1998).

[35] J. P. Perdew and A. Zunger, *Self-Interaction Correction to Density-Functional Approximations for Many-Electron Systems*, Phys. Rev. B **23**, 5048 (1981).

[36] N. Tancogne-Dejean *et al.*, *Octopus, a Computational Framework for Exploring Light-Driven Phenomena and Quantum Dynamics in Extended and Finite Systems*, J. Chem. Phys. **152**, 124119 (2020).

[37] S. A. Sato, Y. Shinohara, T. Otobe, and K. Yabana, *Dielectric Response of Laser-Excited Silicon at Finite Electron Temperature*, Phys. Rev. B **90**, 174303 (2014).

[38] H.-J. Hagemann, W. Gudat, and C. Kunz, *Optical Constants from the Far Infrared to the X-Ray Region: Mg, Al, Cu, Ag, Au, Bi, C, and* $Al_2O_3$, J. Opt. Soc. Am. **65**, 742 (1975).

[39] C. Kittel, *Introduction to Solid State Physics*, 8th ed. (John Wiley & Sons, New York, NY, 2004).

[40] G. D. Mahan, *Condensed Matter in a Nutshell*, 8th ed. (Princeton University Press, 2011).

[41] J. I. Mustafa, M. Bernardi, J. B. Neaton, and S. G. Louie, *Ab Initio Electronic Relaxation Times and Transport in Noble Metals*, Phys. Rev. B **94**, 155105 (2016).